



HAL
open science

Fast Computing Flow Battery Modeling to Optimize the Choice of Electrolytes and Operating Conditions – Application to Aqueous Organic Electrolytes

Quentin Cacciuttolo, Martin Petit, David Pasquier

► To cite this version:

Quentin Cacciuttolo, Martin Petit, David Pasquier. Fast Computing Flow Battery Modeling to Optimize the Choice of Electrolytes and Operating Conditions – Application to Aqueous Organic Electrolytes. *Electrochimica Acta*, 2021, 392, pp.138961. 10.1016/j.electacta.2021.138961 . hal-03353804

HAL Id: hal-03353804

<https://ifp.hal.science/hal-03353804>

Submitted on 24 Sep 2021

HAL is a multi-disciplinary open access archive for the deposit and dissemination of scientific research documents, whether they are published or not. The documents may come from teaching and research institutions in France or abroad, or from public or private research centers.

L'archive ouverte pluridisciplinaire **HAL**, est destinée au dépôt et à la diffusion de documents scientifiques de niveau recherche, publiés ou non, émanant des établissements d'enseignement et de recherche français ou étrangers, des laboratoires publics ou privés.

Fast computing flow battery modeling to optimize the choice of electrolytes and operating conditions – Application to aqueous organic electrolytes.

Quentin Cacciuttolo^{a,1}, Martin Petit^a, David Pasquier^a

^aIFP Energies Nouvelles, Rond-point de l'échangeur de Solaize, BP3, 69390 Solaize, France

Abstract

We have developed a 0D model of aqueous organic redox flow battery to have a better understanding of the impact of oxygen and hydrogen evolution as a parasitic side reaction on the evolution of the battery performances. This lumped approach model is able to account for multiple redox processes at each electrode, which, to our knowledge has not been described in the literature. In this article the study is focused on alkaline battery and the model has been validated on 2,6-dihydroanthraquinone / ferrocyanide electrolytes at laboratory full cell level. The model considers the electrochemical reactions, the electrolyte flow rate, the diffusion of the electroactive molecules from the bulk to the reaction sites, the transfer of cations through a perfluorosulfonic membrane and the ohmic losses. Furthermore, the electrochemical reactions accounted for include the reduction and the oxidation of water modeled with Tafel slopes. Thanks to this approach, we highlight the non-negligible role of oxygen evolution reaction in these conditions. The model is used as a tool to optimize operating conditions as well as to predict the most advantageous potential of electrolytes to enhance performances and limit side reactions. For example, under alkaline condition (pH=14), the negolyte standard potential can be targeted to -0.8 V without competing with HER, however, the posolyte potential must be kept below 0.65 V to avoid competition with OER.

Introduction

Nowadays, electric grids, from microgrid to continental scale network, include an increasingly important proportion of low carbon issuer but fluctuating power productions (solar, wind, stream turbine...). These variable productions are not correlated with power consumption and trend to destabilize the power grid and can lead to shutdowns. Therefore, the need of electric energy storage (EES) is growing with the evolution of grids. Depending on dynamic response and power and energy capacities, EES can provide different grid services: grid support services, frequency regulation, renewable penetration in isolated areas, rural electrification, solution for self-consumption, critical customer's needs... Redox flow batteries (RFB) are an attractive electrochemical energy storage that can store large amounts of energy and power (up to MW/MWh), has a fast response time and high and decoupled current and power performances.

A schematic representation of RFB is given in Figure 1. In RFB, energy is stored in two liquid electrolytes containing electrochemically active species: posolyte and negolyte. Electrolytes are pumped from tanks to electrochemical cells. These cells consist of two compartments containing porous electrodes, separated by a membrane. Electrolyte flow through electrodes

¹ Corresponding author

where electrochemical reactions are taking place. During charge, posolyte is oxidized and negolyte reduced. Reverse reactions involve during discharge. The membrane isolates the two electrolytes while allowing the ion transfer necessary for charge balance. The energy stored depends on the electrolyte volume and the achievable power is related to the number and surface area of the electrochemical cells.

The most developed RFBs use metal based electroactive materials (vanadium (VRFB), iron/vanadium, zinc/bromine redox flow battery...) [1]. These systems are however limited by cost and low abundance of electroactive materials, environmental and safety concerns (e.g. formation of Br₂ in bromine flow battery) and performance constraints (high corrosiveness, high crossover) which make it difficult for them to achieve competitiveness with other storage systems [1].

In parallel to the development of commercial VRFB, a new family of RFB is rising using organic electroactive species (ORFB) in aqueous or organic solvent. Aqueous ORFB (AORFB) could alleviate issues listed above on VRFB. Electrolytes in AORFB are based on different chemical families such as quinone, viologen, TEMPO or alloxazine [1,2]. An important amount of new molecules have been recently synthesized and tested with a large range of electrochemical properties (standard potential, kinetics), transport properties (diffusion coefficient), water solubilities and stabilities [2–5].

Similarly, as for Li-ion batteries or fuel cells, models and simulations have been reported to describe the electrochemical behavior of VRFB and other metallic/halide RFBs. The scale and complexity of the models depend on the intended use. Molecular models such as DFT make it possible to predict intrinsic material properties such as redox potential, chemical stability or solvation energy [6,7]. Physical models at cell or stack level allow to have a better understanding on different phenomena such as crossover, [8–15] effect of microstructure [16,17] or operating conditions [18–26]. CFD models help to optimize the design of cells and stacks in order to ensure homogeneous flow distribution or minimizing either pressure drops or shunt current in stacks [27–30]. Empirical models describe at macro level the battery behavior and so request less calculation time. They are therefore used for estimating state of charge or state of health, monitoring and control or integrated in larger system modeling, up to energy management system [31–36].

At the step of AORFB technology development, simulations have not been yet widely used. Except DFT which is a useful tool in molecular engineering of new electrolytes [37–39], only Zhang *et al.* propose a 3D steady state lattice Boltzmann model of ORFB with TEMPO in acetonitrile to study different electrode structures [40], Li a 3D steady state model on 9,10-anthraquinone-2,7-disulfonic acid/Br system [41] and Chen *et al.* a 1D model of electrode to investigate voltage losses [42].

In general, models do not manage to accurately represent the capacity losses observed during cycling, because the physical mechanisms responsible for this capacity fade are not considered in the model. Unbalancing is among the main phenomena responsible for this capacity fade and is often correlated with the presence of secondary reactions. Consequently, for a given system, the optimisation of experimental conditions, especially the nominal voltage range, is

done by successive trial and error in order to identify a good compromise between long-term stability and energy density and efficiency.

In the present work, we have developed a 0D physical model of an AORFB cell taking into account solvent side reactions, such as oxygen evolution reaction (OER) and hydrogen evolution reaction (HER). In our approach, the model is able to account for multiple redox processes allowing in the present case to simulate the HER and OER reactions occurring simultaneously and which can reduce the faradic efficiency and unbalancing the system. In this paper the case of alkaline AORFB is considered. For this study, the electrolytes tested as reference electrolytes for the validation of the model are 2,6-dihydroxyanthraquinone (2,6-DHAQ) and ferrocyanide studied in details by Lin *et al* [43]. Thanks to the model, we will investigate the role of HER and OER side reactions in long term performances of AORFB and try to determine the better threshold in terms of electrolyte potential between a high energy dense AORFB and performance degradation related to HER and OER at different operating conditions. In such anthraquinone/ferrocyanide system, the crossover can be neglected in comparison with chemical and electrochemical degradations and HER/OER side reactions occurring at non controlled operating conditions [44,45]. Further work will focus on the specific effect of electrochemical and chemical degradation of electrolyte.

Experimental Description

In order to provide this study with accurate and repeatable results for model, calibration and validation a posolyte/negolyte couple have been chosen and operated in a dedicated flow cell. Both electrolytes systems and flow cells are described in this part.

Electrolytes formulation

Anhydrous potassium ferrocyanide (Acros Organic, purity 99+%), KOH (Merck, analytical grade) and 2,6-DHAQ (MuseChem, purity 97.2 %) are used as received. 0.5 M 2,6-DHAQ Negolyte is prepared by dissolving 2,6-DHAQ powder in KOH 2M. Similarly, 0.4 M potassium ferrocyanide posolyte is based on a KOH 1M solution. Ferrocyanide based electrolytes is prepared and used in tinted glass to protect them from possible photochemical degradation.

Flow battery experimental set-up

Test in full cell have been performed in a flow cell set up presented in Figure 2 and supplied by Pinflow. This set up is a sandwich constituted from outside to inside of two metallic/PVC frames for mechanical maintain, two copper current collectors separated from the porous carbon felt electrodes by two composite carbon plates, two PVC frames with inside channels allowing the electrolyte circulation and N115 Nafion® membrane separating the both symmetrical parts of the cell. Gaskets are placed between membrane and PVC frames and between PVC frames and current collector. The device once assembled consists in two sealed compartments each containing a porous electrode and a circulating electrolyte separated by a membrane. Geometrical dimensions are gathered in Table 2. Peristaltic pumps are used for the circulation of electrolyte with a flow rate between 10 and 16 mL·mn⁻¹. Inert N₂ atmosphere is maintained in the electrolyte tanks.

In order to evaluate Tafel parameters for HER and OER on carbon felts used in the flow cell, one carbon electrode is replaced by a platinized titanium electrode. Polarization curves are recorded using a 1M KOH electrolyte with a flow rate of 16 mL·mn⁻¹ and a scan rate of 10 mV·s⁻¹

¹. Except electrode materials, the cell is identical than the one used as flow battery described above. At low current density ($< 5 \text{ mA}\cdot\text{cm}^{-2}$), only ohmic and reaction kinetics overvoltage at carbon electrode are considered to be current limiting. Ohmic resistivity of the cell and membrane in KOH 1M have been determined by electrochemical impedance spectroscopy and is approximatively 0.59Ω . Tafel curves are drawn in Figure S3 for each reaction in order to measure specific kinetic parameters for these conditions of cell, pH and carbon felt electrode.

Experimental cycling protocols

The electrical testing of the system is performed using a Biologic MPG205 potentiostat. Electrical cycling serves two aims in this study, model calibration first and then model validation.

First of all, charge and discharge cycles are performed in order to assess the behavior of the system on the whole state of charge range and calibrate main parameters of the model.

The cycles parameters being charge and discharge current densities as well as voltage range can be changed in order to fit with electrolyte requirements. The battery capacity is estimated through coulometry during discharge.

Once the model calibrated, it is validated thanks to dedicated power duty cycles representative of the final application. The two duty cycles used in this study were proposed by the PNNL [46] in order to represent realistic cycling conditions in stationary microgrid applications. The battery is set at medium state of charge before the duty profile is applied. It has been scaled initially in order to match the expected battery performances. In the case of this study the scale ratio used is 1 W.

Model Description

Several modelling approaches are possible for flow battery behavior simulation at various scales from material to the complete system. At cell level the most simple one are based on electrical equivalent circuits which can take into account some physical parameters such as species concentrations [31]. However, these kinds of model are intrinsically less predictive as many physical phenomena are not correctly considered.

In order to understand the inner behavior of flow batteries and allow further interpretations such as performance degradation and molecule screening, an electrochemical modelling has been adopted, since such an approach does not rely entirely on experimental data and allow thus extrapolation.

Electrochemical modelling of flow batteries has been developed over the past years based on the ground work of fuel cell models previously settled [23]. Most modelling studies focus on vanadium flow batteries taking into account most relevant phenomena occurring in such systems, such as main electrochemical reactions [23], parasitic reactions such as oxygen and hydrogen formation [24,25], crossover of vanadium species and water through the membrane [8,26], some specific overvoltage due to ion concentration discontinuity near the membrane [15,19] or the thermal behavior of flow batteries [15]. Most of these approaches are based on 2D modelling implemented into a finite element modeling platform. As a consequence, computational time required is quite high and prevents studying long term behavior such as performance degradation over several years or an extensive parametric study.

In order to reduce computational times, a simplified approach has been developed where both cell compartments are considered as being uniform in terms of potentials and concentrations. This approach is taken for this work and is similar to the one chosen by Boettcher et al. [8]. The aim is to focus on the chemical and electrochemical behavior of the studied systems. A versatile modelling framework has then been developed using R programming language and DEsolve ODE solving package [47].

The main assumptions of this approach are the following:

- Uniform concentration in the cell compartment and within the tanks,
- Adiabatic condition,
- The species taken into account in this study are: hydroxide ion OH^- , deprotonated 2,6-dihydroxyanthraquinone $DHAQ^{2-}$, deprotonated 2,6-dihydroxyanthrahydroquinone $DHAHQ^{4-}$, ferrocyanide $Fe(CN)_6^{3-}$, ferricyanide $Fe(CN)_6^{4-}$, potassium ion K^+ , dioxygen O_2 and dihydrogen H_2 ,
- Activity of species in solution are approximated with concentration,
- Negligible ohmic losses in the solid phase as well as in the electrolytic phase in the compartments,
- Resident time in tubing is neglected
- Only HER and OER are considered as side reactions,
- No crossover occurs through the membrane.

Under these assumptions, the cell voltage is computed as follows similarly to the SPM approaches in Li-ion batteries [48]:

$$U_{cell} = \phi_s^+ - \phi_s^- = \Delta\phi^+ + \eta_{ohm}^{s+} + \eta_{ohm}^{e+} + \eta^{mem} - \Delta\phi^- - \eta_{ohm}^{s-} - \eta_{ohm}^{e-} \quad \text{Eq. 1}$$

In this equation, $\Delta\phi^+$ and $\Delta\phi^-$ are the differences between solid and electrolytic potentials in respectively the positive and negative electrodes, η_{ohm}^s is the ohmic overpotential due to the mean ohmic drop between the collector and the membrane, η_{ohm}^e the overpotential between the mean electrolyte potential between the current collector and the membrane and the membrane electrolytic potential. All these can be expressed as follows

$$\Delta\phi^\pm = \overline{\phi_s^\pm} - \overline{\phi_e^\pm} \quad \text{Eq. 2}$$

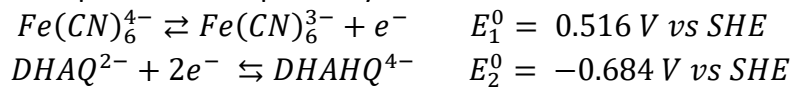
$$\eta_{ohm}^s = \overline{\phi_s^\pm} - \overline{\phi_s} \approx 0 \quad \text{Eq. 3}$$

$$\eta_{ohm}^e = \overline{\phi_e} - \overline{\phi_e^\pm} \approx 0 \quad \text{Eq. 4}$$

$$\eta_{mem} = \phi_e^{mem+} - \phi_e^{mem-} \quad \text{Eq. 5}$$

Main electrochemical reactions and reference potentials

The main electrochemical reactions occurring in the system are the following for the positive and the negative compartments respectively:



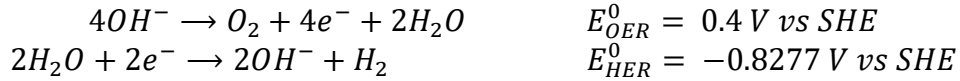
In these equations, charge reactions are indicated from left to right and discharge reaction from right to left. In the chosen alkaline conditions, hydroxy functions of 2,6-dihydroxyanthraquinone and 2,6-dihydroxyanthrahydroquinone are fully deprotonated.

Hence, this means no water is involved in these electrochemical reactions as it is schematized in Figure S1. Depending on active specie concentrations, reference potential of each reaction occurring in the compartments can be computed based on Nernst law as follows:

$$E_{ref}^1 = E_1^0 + \frac{RT}{\mathcal{F}} \ln \left(\frac{[Fe(CN)_6^{3-}]}{[Fe(CN)_6^{4-}]} \right) \quad \text{Eq. 6}$$

$$E_{ref}^2 = E_2^0 + \frac{RT}{2\mathcal{F}} \ln \left(\frac{[DHAQ^{2-}]}{[DHAHQ^{4-}]} \right) \quad \text{Eq. 7}$$

Moreover, some other parasitic reactions occur in aqueous solvent such as oxygen and hydrogen evolution reactions as follows:



With following reference potentials:

$$E_{ref}^{OER} = E_{OER}^0 + \frac{RT}{4\mathcal{F}} \ln \left(\frac{[O_2]}{[OH^-]^4} \right) \quad \text{Eq. 8}$$

$$E_{ref}^{HER} = E_{HER}^0 + \frac{RT}{2\mathcal{F}} \ln \left(\frac{1}{[OH^-]^2[H_2]} \right) \quad \text{Eq. 9}$$

Charge transfer kinetics

The first overpotential in Eq. 2 is linked to the charge transfer between the solid phase and the liquid phase. Following what is being done in Li-ion batteries modelling [49], it is computed using a double layer capacitance which is charged based on the balance between electrochemical reactions currents and the input current as follows:

$$\frac{d\Delta\phi}{dt} = \frac{1}{a_s C_{dl}} \left(\frac{I}{Vol_{comp} \varepsilon_{comp}} - \sum j_f^i \right) \quad \text{Eq. 10}$$

In this expression, C_{dl} is the double layer capacitance, Vol_{comp} is the volume of the compartment in m^3 , ε is the compartment porosity and a_s is the specific area in m^{-1} . The electrochemical charge transfer currents are computed according to relevant electrochemical kinetics.

For main electrochemical reactions involved in charge and discharge of the battery, Butler-Volmer kinetics is chosen:

$$\begin{aligned} j_f^i &= k^i a_s \mathcal{F} C_{red}^{\alpha^i} C_{ox}^{1-\alpha^i} \left(\frac{C_{red}^S}{C_{red}} \exp \left(\frac{\alpha^i \mathcal{F} (\Delta\phi - E_{ref}^i)}{RT} \right) \right. \\ &\quad \left. - \frac{C_{ox}^S}{C_{ox}} \exp \left(- \frac{(1 - \alpha^i) \mathcal{F} (\Delta\phi - E_{ref}^i)}{RT} \right) \right) \end{aligned} \quad \text{Eq. 11}$$

In this expression representing the current density for the reaction i , α^i , C_{ox} and C_{red} are respectively charge transfer coefficient, the concentration of oxidizer and the concentration of the reducer and the subscript S is used to represent the concentration at the felt surface

whereas in its absence, the bulk concentration is considered. To evaluate the surface concentration of the specie j , linear equations system balancing the mass transfer from the bulk to the surface with charge transfer is solved as follows:

$$a_s \mathcal{F} k_{ml} (C_j - C_j^S) = \sum_i v_{j,ox}^i j_f^i - \sum_i v_{j,red}^i j_f^i \quad \text{Eq. 12}$$

To represent mass transfer between the bulk and the surface, the transfer coefficient k_{ml} is used (expressed in $\text{m}\cdot\text{s}^{-1}$). $v_{j,ox}$ and $v_{j,red}$ are the stoichiometric coefficients of the specie j in reactions where j is respectively an oxidizer and a reducer for 1 exchanged electron. For instance, in the case of $DHAQ^{2-}/DHAHQ^{4-}$ reaction, $v_{DHAQ^{2-},ox}^2$ is 0.5 and $v_{DHAQ^{2-},red}^2$ is 0 and $v_{DHAHQ^{4-},ox}^2$ is 0 and $v_{DHAHQ^{4-},red}^2$ is 0.5.

In this case $DHAQ^{2-}$ is the oxidizer of reaction 2, if $\eta > E_{ref}^2$, then an oxidation leads to $DHAQ^{2-}$ formation, j_f^2 is positive and $[DHAQ^{2-}] > [DHAQ^{2-}]^S$.

k_{ml} is linked to the diffusion coefficient D_i and the pore size d_f [50], $k_{ml} = \frac{D_i}{d_f}$.

For hydrogen and oxygen evolution reactions (HER and OER), a Tafel kinetic formulation is used representing irreversible electrochemical reactions for the whole felt as follows:

$$j_f^i = i_0^i \exp(\beta^i (\Delta\phi - E_{ref}^i)) \quad \text{Eq. 13}$$

i_0^i is the exchange current density of the reaction i and β^i is its Tafel slope.

Electrolytic overvoltages

Electrolytic overvoltages are the third and fourth overvoltages presented in Eq. 4 and Eq. 5.. Ohmic electrolytic overpotential is neglected due to high conductivity of aqueous solutions. However, the membrane causes 2 main voltage drops during the battery operation.

The first one is the Donnan potential due to the ionic concentration discontinuity at the membrane electrolyte boundary. It can be expressed similarly to the Nernst equation. With the hypothesis of uniform ionic concentrations in the membrane, the global Donnan potential as mentioned by Knehr et al. [51] for protons is:

$$\eta_{Donnan} = \frac{RT}{\mathcal{F}} \ln \left(\frac{[K_{pos}^+]}{[K_{neg}^+]} \right) \quad \text{Eq. 14}$$

The second overpotential is due to the ohmic losses in the membrane. It can be expressed using the conductivity of the membrane, σ_{mem} , as follows:

$$\eta_{ohm}^{mem} = \frac{\delta_{mem}}{\sigma_{mem} A_{mem}} I_{elec} = R_{mem} I_{elec} \quad \text{Eq. 15}$$

In this expression, A_{mem} is the membrane area, δ_{mem} is the membrane thickness, and I_{elec} is the global electrolytic current. The value of this overpotential has been calibrated because of the difficulty to estimate δ_{mem} and σ_{mem} depending on water swelling.

Consequently, the global overvoltage in the membrane is the following

$$\eta_{mem} = \eta_{ohm}^{mem} + \eta_{Donnan} \quad \text{Eq. 16}$$

Mass balance in the compartments

Due to electrochemical reactions, the concentrations of species are modified along the reactive volume. It is then possible to evaluate the output concentration based on the input concentrations and the reaction currents using the plug flow assumption as follows:

$$C_{out}^j = C_{tank}^j + \frac{\varepsilon_{comp} Vol_{comp}}{\mathcal{F} Q_{comp}} \sum_i \frac{\nu_j^i}{n_e^i} j_f^i \quad \text{Eq. 17}$$

In this expression ν_j^i is the stoichiometric coefficient of the specie j in reaction i and is positive if j is the oxidizer and negative if it is the reducer, n_e^i is the number of electrons exchanged in the reaction i . ε_{comp} is the carbon felt porosity, Vol_{comp} is the compartment volume and Q_{comp} , the compartment flow-rate so that $\frac{\varepsilon_{comp} Vol_{comp}}{Q_{comp}}$ is the transit time in the compartment.

To ensure electroneutrality in both compartments, K^+ is transferred through the membrane using the concentrations computed in the former equation in both compartments.

$$\Delta C_{out}^{K^+} = \sum_j z_j C_{out}^j \quad \text{Eq. 18}$$

Finally, this term is added to both compartments for calculating the output concentration for K^+ to account for ionic transport in the membrane.

Tanks modelling

Tanks are modelled as perfectly stirred reactors whose concentrations only varies depending on the feeding rate of product from the cell. The variation of tank concentration, as formulated by Shah et al. [25] is given by:

$$\frac{dC_{tank}^j}{dt} = \frac{Q}{V_{tank}} (C_{out}^j - C_{tank}^j) \quad \text{Eq. 19}$$

In this expression, Q is the electrolyte flowrate and V_{tank} is the tank volume.

Model implementation

The model has been coded using R and the DESolve package and especially the Isodar solver [47]. This solver allows an automated switch between stiff and non-stiff methods and also the use of a root function to change the operating conditions depending on voltage and current measurements. According to these roots and events, the operating modes are automatically changed among 6 states as described in Table 1. Depending on the cycling definition, the state order can vary. The parameter τ is the characteristic time for current calculation during constant voltage phase. In this study, it is fixed to 0.001 s in order to ensure a fast transition between the constant current set point and the current needed to ensure a constant voltage as well as reasonable calculation time. t_{state} is the time elapsed after the beginning of the state.

Table 1: Operating state of the cell in the model

State number	State	Operating condition	End condition
1	Charge	$I = I_{ch}$	$U = U_{max}$
2	Discharge	$I = I_{dch}$	$U = U_{min}$

3	Constant voltage charge	$\frac{dI}{dt} = \frac{1}{\tau} (U_{max} - U)$	$ I < I_{lim}$
4	Constant voltage discharge	$\frac{dI}{dt} = \frac{1}{\tau} (U_{min} - U)$	$ I < I_{lim}$
5	Rest after charge	$I = 0$	$t_{state} > t_{rest}$
6	Rest after discharge	$I = 0$	$t_{state} > t_{rest}$
7	Power profile	$I = f(t_{state})$	$t_{state} > t_{profile}$

The state variables of this model are:

- η_{pos} and η_{neg} ,
- The tank concentrations (8 species),
- The cell voltage U ,
- The cell current I ,
- The discrete state in which the system is.

The solver allows a seventh states where the battery is controlled with an imported power profile.

Parameters

Main parameters have been obtained either in literature, measured or calibrated. Geometric parameters regarding the experimental set-up have been measured directly or taken from the material provider datasheet and are gathered in Table 2. Reaction parameters are given in Table 4. Electrochemical and kinetics parameter of 2,6-DHAQ and ferrocyanide have been determined by Lin *et al.* on glassy carbon [43] but had to be calibrated for carbon felt electrodes. Furthermore, diffusion coefficient of electrolyte species has been calibrated to take into account the concentrated solution and confined media. This explains why values are slightly different from experiment data found in the literature [43]. Parameters for HER and OER have been fitted to experimental polarization curves obtained thanks to carbon/platinum coated titanium flow cell. These curves are represented in Figure S3. Finally, diffusion coefficient summarized in Table 3 and membrane conductivity have been optimized to fit with experimental data. Figure 3 present the fitted model and experimental data on one cycle with the conditions described in the next paragraph.

Table 2: Geometric parameters

V_{comp}	40 x 50 x 3 mm ³
ϵ_{comp}	0.93
d_f	10 μ m
a_s	35000 m ² /m ³
δ_{mem}	125 μ m
A_{mem}	20 cm ²

Table 3: Charge and mass transport parameters

$D^{DHAQ^{2-}}$	$1.7 \cdot 10^{-5} \text{ m}^2 \cdot \text{s}^{-1}$	calibrated
$D^{DHAHQ^{4-}}$	$1.4 \cdot 10^{-10} \text{ m}^2 \cdot \text{s}^{-1}$	calibrated
$D^{Fe(CN)_6^{3-}}$	$2.7 \cdot 10^{-7} \text{ m}^2 \cdot \text{s}^{-1}$	calibrated

$D^{Fe(CN)_6^{4-}}$	$1.9 \cdot 10^{-10} \text{ m}^2 \cdot \text{s}^{-1}$	calibrated
R_{mem}	$1.0 \cdot 10^{-1} \Omega$	calibrated

Table 4: Reaction parameters

$E_{DHAQ^{2-}/DHAHQ^{4-}}^0$	-0.684 V vs SHE	[43]
$E_{Fe(CN)_6^{3-}/Fe(CN)_6^{4-}}^0$	0.516 V vs SHE	[43]
E_{O_2/HO^-}^0	0.4 V vs SHE	[52]
E_{H_2O/H_2}^0	-0.8277 V vs SHE	[52]
$\alpha^{DHAQ^{2-}/DHAHQ^{4-}}$	0.5	[43]
$\alpha^{Fe(CN)_6^{3-}/Fe(CN)_6^{4-}}$	0.5	[43]
$k^{DHAQ^{2-}/DHAHQ^{4-}}$	$7.0 \cdot 10^{-5} \text{ m} \cdot \text{s}^{-1}$	calibrated
$k^{Fe(CN)_6^{3-}/Fe(CN)_6^{4-}}$	$3.3 \cdot 10^{-5} \text{ m} \cdot \text{s}^{-1}$	calibrated
β^{OER}	$13.6 \text{ V} \cdot \text{dec}^{-1}$	Experimentally determined
β^{HER}	$-12.0 \text{ V} \cdot \text{dec}^{-1}$	Experimentally determined
i_0^{OER}	$3.1 \cdot 10^{-5} \text{ A/carbon felt}$	Experimentally determined
i_0^{HER}	$2.6 \cdot 10^{-8} \text{ A/carbon felt}$	Experimentally determined

Initial conditions

The system is initialized with a cell almost fully discharged. Initial concentrations are given in Table 5. The initial state is the state 1 (constant current charge). The system is at rest at the beginning of the simulation with positive and negative overvoltage being equal to the equilibrium potential of the main reactions, so that no reaction occurs. At equilibrium, charged specie concentrations are set to $1 \text{ mol} \cdot \text{m}^{-3}$ to avoid division by 0 in Nernst equation. Initial overpotential $\Delta\phi$ are evaluated to be equal to equilibrium potential in initial concentration conditions.

Table 5: Initial conditions

Parameter	Posolyte	Negolyte
$[OH^-]_0$	$1000 \text{ mol} \cdot \text{m}^{-3}$	$1000 \text{ mol} \cdot \text{m}^{-3}$
$[DHAQ^{4-}]_0$	$0 \text{ mol} \cdot \text{m}^{-3}$	$1 \text{ mol} \cdot \text{m}^{-3}$
$[DHAHQ^{2-}]_0$	$0 \text{ mol} \cdot \text{m}^{-3}$	$500 \text{ mol} \cdot \text{m}^{-3}$
$[Fe(CN)_6^{3-}]_0$	$400 \text{ mol} \cdot \text{m}^{-3}$	$0 \text{ mol} \cdot \text{m}^{-3}$
$[Fe(CN)_6^{4-}]_0$	$1 \text{ mol} \cdot \text{m}^{-3}$	$0 \text{ mol} \cdot \text{m}^{-3}$
$[K^+]_0$	$1000 \text{ mol} \cdot \text{m}^{-3}$	$1000 \text{ mol} \cdot \text{m}^{-3}$
$[O_2]_0$	$0 \text{ mol} \cdot \text{m}^{-3}$	$1 \text{ mol} \cdot \text{m}^{-3}$
$[H_2]_0$	$0 \text{ mol} \cdot \text{m}^{-3}$	$1 \text{ mol} \cdot \text{m}^{-3}$
$\Delta\phi$	0.362 V	-0.575 V
State	6	
U	0.937 V	
I	I_{ch}	

Model Validation

To validate model and optimized data, simulated cell potential and current with a specific power profile have been compared with experimental data in Figure 4. This power profile of duty cycle signal for frequency regulation applications corresponds to the protocol recommended by PNNL for uniformly measuring and expressing the performance of energy storage systems adapted to the flow cell size (20 cm²) [46] represented in Figure S2. Initial concentrations are calibrated to have the good initial potential (SOC 80 %).

Both, simulated voltage and cell current is fitting correctly experimental data with an error lower than 0.5 %. The aim of the model is to focus on capacity loss related to HER and OER.

Calculation of optimized potential and operating condition

To increase the performances of a system, or to look at new chemistries increasing the storage system performances, several parameters can be optimized such as the operating voltage range or the standard potential of the used species. However, especially in aqueous systems, such adjustment may lead to adverse phenomena leading to decreased energetic or columbic efficiencies or reduced cycling capabilities. By using the developed model, it is possible to assess long term behavior of the system and thus figure out optimized operating conditions.

Performances tested

In order to study the effect of parameter's sensitivity on performance evolution of the RFB, calculated performances are compared along 50 charge and discharge cycles. A cycle consists in the following sequence of states described earlier:

State 6 → State 1 → State 3 → State 5 → State 2 → State 4 → State 6

This sequence is repeated during 430 h to achieve more than 50 cycles. Evolution of current density, cell voltage, potentials of negative and positive electrodes, capacity and energy during each cycle and concentration of the different species in the both negative and positive tanks are recorded. For example, Figure 5 and Figure 6 represent respectively the evolution of current density and cell voltage and the evolution of the concentration of the different species in the reference case (corresponding to 2,6-DHAQ / Ferrocyanide cell tested experimentally). Cell voltage is kept between $U_{\min} = 0.6$ V and $U_{\max} 1.6$ V and current density between -37.5 and 37.5 mA·cm⁻².

The discharge capacity and energy at each cycle is presented in Figure 7. The value of first cycle discharge capacity (1536 mA·h) is lower than theoretically expected (2144 mA·h) due to diffusion limitation at the electrode combined with kinetics limitations leading to high overpotentials which fasten the reaching of U_{\min} and U_{\max} . As it could be noted in Figure 6, not all $\text{Fe}(\text{CN})_6^{3-}$ ions have been fully oxidized and, respectively, not all 2,6-DHAQ²⁻ species have been reduced during charge and similarly charged species have not be totally transformed during the discharge. At each cycle, the capacity of the battery decreases slowly. Capacity fade is around 0.06 % per cycle. Thanks to the model, this phenomenon can be directly linked to a parasitic reaction producing oxygen instead of the oxidized positive specie. In fact, no degradation of species and no crossover is taken into account in the model. In these conditions, HER is not involved.

The model simulates several conditions to understand the significance of controlling these reactions which are directly related to the catalytic properties of carbon felts and the potential limits of new electroactive species.

i_0^H , i_0^O , U_{min} , U_{max} , E_1^0 and E_2^0 are set as adjustable parameters to simulate, respectively, a change of catalytic properties of carbon felts, operating conditions and new electroactive species with different potentials. The relative impact of these parameters on capacity and energy evolution is then followed. For many different conditions, the evolution of these values during cycling is compared at cycle 2 in case of energy and capacity, between cycle 2 and cycle 50 in case of energy retention, and at cycle 2 as for energy efficiency.

Increase of HER and OER exchange current densities

By increasing i_0^H and i_0^O , a change of catalytic activity respectively of HER and OER on the carbon felt is simulated. Carbon felt is a really poor catalyst for both reactions which allows working with electrolyte with such reference potential. In the case of VRFB, special work is carried out on carbon felt to modify surface properties and increase wettability and interaction with electroactive species, resulting in improved performances [53–59]. Inspired by these works, similar improvement could be initiated on AORFB. However, this treatment has to avoid any enhancement of catalytic activity towards OER. Figure 7 presents the evolution of capacity, energy, faradic efficiency and energy efficiency during 50 cycles with three values of i_0^O . With the actual experimentally measured i_0^O implemented in the model, a slightly decrease of capacity and energy (respectively –3.1% and –3.1%) is observed after 50 cycles. If i_0^O is divided by 10, the evolution of capacity and energy by cycle remain stable. On the contrary, if i_0^O is multiplied by 100, the battery performances drop consequently as well as the energy efficiency. Oxidation of ferrocyanide is in stronger competition with OER. The control of a low i_0^O , so a low kinetics, is essential to decrease capacity loss during cycling in this alkaline condition where OER standard potential is shifted towards lower potential and the reaction thermodynamically favored. The experimentally tested conditions are not yet ideal and could be improved by slightly decreasing the electrode activity towards OER.

The effect of i_0^H on the evolution of capacity and energy during cycling is different. Similarly to the Figure 7, Figure 8 shows the evolutions of capacity, energy, faradic efficiency, energy efficiency during 50 cycles with different i_0^H . In reference conditions, HER is negligible. Increasing this parameter has no effect until it is multiplied by a factor 10 000. Capacity and energy increase cycle by cycle with this value of i_0^H . With a 100,000 times higher i_0^H , the increase is even greater and reaches maximum capacity and energy of 1806 mA·h (at cycle 16) and 1454 mW·h (at cycle 20) respectively.

An explanation of this behavior could be highlighted with the evolution of electroactive species concentrations during cycling in this particular condition presented in Figure 9. As observed in Figure 6, the first charge is limited by diffusion and not all the electroactive species are converted during the charge and the discharge. When HER appears more preponderant, the amount of $\text{Fe}(\text{CN})_6^{3-}$ increases, charge after charge, until total conversion of $\text{Fe}(\text{CN})_6^{4-}$ after 20 cycles. This phenomenon is made possible because HER occurs at negative electrode, creating an unbalance between both electrolytes. Whereas not all the electroactive species are fully electrochemically transformed this unbalance allows an increase of both capacity and

energy of the battery. Then unbalancing continues to worsen. The electrons consumed by HER during the charge cannot be returned to the system during discharge, so that the capacity and the energy of the battery decrease.

Optimization of operating window

Considering HER et OER, operating potential limits are a trade-off between converting a maximum amount of electrolyte and limiting HER and OER current losses and thus between maximized capacity and energy efficiency. Several U_{\min} and U_{\max} have been numerically tested between 0.4 and 0.7 V and between 1.5 and 1.8 V respectively. For each operating condition, capacity and energy recovered during discharge of the second cycle, energy efficiency at cycle 2 and energy retention between cycle 50 et 2 are compared in Figure 10. Each of these values has a specific trend depending on the values of U_{\min} and U_{\max} :

- Energy increases strongly when U_{\min} increases, and slightly with increasing U_{\max} , reaching a maximum at 1242 mW·h,
- Capacity increases strongly with U_{\max} between 1.50 and 1.60 V, remains stable beyond and toward U_{\min} and reaches a maximum at 1536 mA·h,
- Energy retention remains roughly constant around 95.8 % with a small decrease when decreasing U_{\min} and increasing U_{\max} ,
- Energy efficiency falls from 54 % to 40 % when lessening U_{\min} and increasing U_{\max} .

When U_{\max} increases, a larger amount of active species will be transformed leading to a capacity increasing. No influence of U_{\min} on capacity denotes that limitation in converting electroactive substance mainly appears during charge and that HER is not encountered. Energy decreases logically with U_{\min} by definition ($E = \int U I dt$). Furthermore, energy efficiency drops when U_{\min} decreases and U_{\max} increases because more energy is brought to the battery to charge it and less is recovered during the discharge.

Finally, operating conditions applied experimentally ($U_{\min} = 0.6$ V, $U_{\max} = 1.6$ V) are still a good trade-off to maximize these values but not the most optimized. A higher U_{\min} could be more accurate to increase both energy and energy efficiency, without decreasing capacity.

The model also allows to screen a large number of different couples of molecules in order to optimize operating conditions. For a given molecule, the only parameters needed to feed the model are standard potential, kinetic and diffusion coefficient. For example, we simulated fictitious molecules with different potential for the two electrolytes, while considering kinetics and diffusion coefficient equal to those of 2,6-DHAQ and ferrocyanide respectively. Furthermore, U_{\min} and U_{\max} are adjusted considering the variation of electrolyte potentials.

Figure 11 and Figure 12 represent the result of these simulations. Simulated energy, capacity and energy efficiency at cycle 2 and energy retention between cycles 2 and 50 are represented as a function of negolyte and posolyte standard potentials. For both figures, two conditions are compared: respectively $U_{\min} = 0.6$ V and $U_{\max} = 1.6$ V (identical to experimental conditions) and $U_{\min} = 0.7$ V and $U_{\max} = 1.7$ V in Figure 11 and $U_{\min} = 0.8$ V and $U_{\max} = 1.8$ V in Figure 12.

Considering operating conditions identical to that of experimental ferrocyanide and 2,6-DHAQ system, when E_{neg} and E_{pos} increase in absolute value, the simulation predicts a drop in capacity and energy. This drop is explained by a cell voltage that is not high enough to reach sufficient potential at each electrode to convert all the reagents during the charge. The

capacity drop with the two other imposed potential is thereby reduced respectively by half in the first case and by 80% in the second. Energy and energy efficiency increase by increasing U_{\min} too. By definition, energy at discharge will increase with U_{\min} and so energy efficiency. Regarding energy and energy retention with the highest potential conditions, an optimum electrolyte potential could be reached around $E_{\text{neg}} = -0.8 \text{ V}/E_{\text{pos}} = 0.65 \text{ V}$.

However, this gain of energy at first cycles has to be balanced with the energy retention. After only 50 cycles, energy retention decreases from 95 % to only 75 % when E_{pos} is increased due to a favored OER in such alkaline solution (pH=14). E_{neg} has less effect on this parameter.

HER and OER are yet the only side reactions considered in the model and so this value has to be optimized. Such a 75% energy retention would not be industrially viable. Therefore, ferrocyanide has an optimal standard potential to limit OER in such alkaline conditions. On the other hand, the negative electrolyte potential is not limiting with the 2,6-DHAQ, hence new molecules with lower potential could be considered.

Conclusion

This paper presents a 0D semi-physical model of an aqueous organic redox flow battery (AORFB) at lab cell scale. The model is able to accurately simulate the behavior of the AORFB while accounting for multiple redox processes at the electrodes which is illustrated here with HER and OER parasitic reactions. It has been calibrated and validated on the basis of experimental characterization of a single flow cell using 2,6-DHAQ/ferrocyanide electrolytes. This model has demonstrated its value for optimizing operating condition in terms of energy, capacity and durability against HER and OER. First of all, the model is a useful tool to have a better understanding of the impact of HER and OER on long term tests. It has shown great interest in predicting acceptable potential limits for electrolytes for given conditions (pH, U_{\min} , U_{\max}) or optimizing voltage limits for a given system:

- In alkaline condition (pH = 14), if the maximum voltage is higher than 1.6V, OER has an impact on capacity evolution by unbalancing the SOC between negolyte and posolyte,
- 2,6-DHAQ/ferrocyanide cell optimal cycling conditions are $U_{\min} = 0.8 \text{ V}$ and $U_{\max} = 1.6 \text{ V}$ considering performances and reduction of HER and OER,
- In alkaline condition (pH=14), the negolyte standard potential can be targeted to -0.8 V without being in competition with HER.

To complete this study, a similar approach must be carried out at different pH values (neutral and acidic) and by calibrating the model on experimental data obtained with adapted electrolytes. The pH optimization could be considered in order to limit OER and HER for example and new electrolyte's families could be considered.

One key perspective of this work will be to implement in the model other physical phenomena occurring in flow batteries, in particular, crossover, precipitation and the degradation phenomena that are known to occur on several organic active molecules, the electrodes and the membrane.

Nomenclature

A_{mem}	Membrane surface area, m^2
a_s	Specific surface area, m^{-1}
C	Concentration, $mol \cdot m^{-3}$
C_{dl}	Double layer capacitance, F
C^s	Concentration at the felt surface, $mol \cdot m^{-3}$
D_i	Diffusion coefficient $m^2 \cdot s^{-1}$
d_f	Pore size, m
E^0	Standard potential, V
E_{ref}	Reference potential, V
F	Faraday constant, $96485 C \cdot mol^{-1}$
I	Battery current, A
I_0	Exchange current density, A/carbon felt
I_{elec}	Global electrolyte current, A
j_f	Electrochemical charge transfer current, $A \cdot m^{-2}$
k	Reaction rate constant, $m \cdot s^{-1}$
k_{ml}	Transfert coefficient, $m \cdot s^{-1}$
Q_{comp}	Compartment flow rate, $m^3 \cdot s^{-1}$
R	Gas constant, $J \cdot mol^{-1} \cdot K^{-1}$
R_{mem}	Membrane resistance
U_{Cell}	Cell voltage, V
Vol_{comp}	Volume of compartment, m^3
<i>Greek</i>	
α^i	Charge transfer coefficient in reaction i
β	Tafel slope, $V \cdot dec^{-1}$
δ_{mem}	Membrane thickness, m
ϵ_{comp}	Compartment porosity
η	Overpotential, V
ν_i	Stoichiometric coefficient
σ_{mem}	Membrane conductivity, $S \cdot m^{-1}$
φ	Potential, V
<i>Subscripts and superscripts</i>	
$+$	posolyte
$-$	negolyte
e	Electrolyte phase
mem	Membrane
ohm	ohmic
s	Solid phase or felt surface

References

- [1] J. Winsberg, T. Hagemann, T. Janoschka, M.D. Hager, U.S. Schubert, *Angew. Chem. Int. Ed. Engl.* 56 (2017) 686–711. <https://doi.org/10.1002/anie.201604925>.
- [2] H. Chen, G. Cong, Y.-C. Lu, *Journal of Energy Chemistry* 27 (2018) 1304–1325. <https://doi.org/10.1016/j.jechem.2018.02.009>.
- [3] R. Chen, D. Bresser, M. Saraf, P. Gerlach, A. Balducci, S. Kunz, D. Schröder, S. Passerini, J. Chen, *ChemSusChem* (2020). <https://doi.org/10.1002/cssc.201903382>.
- [4] L.F. Arenas, C. Ponce de León, F.C. Walsh, *Current Opinion in Electrochemistry* 16 (2019) 117–126. <https://doi.org/10.1016/j.coelec.2019.05.007>.
- [5] J. Luo, B. Hu, M. Hu, Y. Zhao, T.L. Liu, *ACS Energy Lett.* 4 (2019) 2220–2240. <https://doi.org/10.1021/acsenerylett.9b01332>.
- [6] R.S. Assary, F.R. Brushett, L.A. Curtiss, *RSC Adv.* 4 (2014) 57442–57451. <https://doi.org/10.1039/c4ra08563a>.
- [7] R.P. Fornari, P. de Silva, *WIREs Comput Mol Sci* 91 (2020) 86. <https://doi.org/10.1002/wcms.1495>.
- [8] P.A. Boettcher, E. Agar, C.R. Dennison, E.C. Kumbur, *J. Electrochem. Soc.* 163 (2015) A5244–A5252. <https://doi.org/10.1149/2.0311601jes>.
- [9] A.R. Crothers, R.M. Darling, D.I. Kushner, M.L. Perry, A.Z. Weber, *J. Electrochem. Soc.* 167 (2020) 13549. <https://doi.org/10.1149/1945-7111/ab6725>.
- [10] L. Hao, Y. Wang, Y. He, *Journal of The Electrochemical Society* 166 (2019) A1310–A1322. <https://doi.org/10.1149/2.1061906jes>.
- [11] K.W. Knehr, E. Agar, C.R. Dennison, A.R. Kalidindi, E.C. Kumbur, *J. Electrochem. Soc.* 159 (2012) A1446–A1459. <https://doi.org/10.1149/2.017209jes>.
- [12] G. Merai, S. Adler, D. Magnor, D.U. Sauer, *Electrochimica Acta* 174 (2015) 945–954. <https://doi.org/10.1016/j.electacta.2015.06.046>.
- [13] D. Jeong, S. Jung, *Int J Energy Res* 44 (2020) 5209–5222. <https://doi.org/10.1002/er.5261>.
- [14] O.C. Esan, X. Shi, Z. Pan, X. Huo, L. An, T.S. Zhao, *Adv. Energy Mater.* 22 (2020) 2000758. <https://doi.org/10.1002/aenm.202000758>.
- [15] Al-Fetlawi, Hassan Abdul-Zehra Abdul-Yima, A.A. Shah, F.C. Walsh, *Electrochim. Acta* 55 (2009) 78–89. <https://doi.org/10.1016/j.electacta.2009.08.009>.
- [16] E. Ali, H. Kwon, J. Choi, J. Lee, J. Kim, H. Park, *Journal of Energy Storage* 28 (2020) 101208. <https://doi.org/10.1016/j.est.2020.101208>.
- [17] G. Aparicio-Mauricio, F.A. Rodríguez, J.J. Pijpers, M.R. Cruz-Díaz, E.P. Rivero, *Journal of Energy Storage* 29 (2020) 101337. <https://doi.org/10.1016/j.est.2020.101337>.
- [18] F.-C. Gu, H.-C. Chen, K.-Y. Li, *Energy Fuels* 34 (2020) 10142–10147. <https://doi.org/10.1021/acs.energyfuels.0c01536>.
- [19] Y. Lei, B.W. Zhang, B.F. Bai, T.S. Zhao, *J. Power Sources* 299 (2015) 202–211. <https://doi.org/10.1016/j.jpowsour.2015.08.100>.
- [20] Y. Li, M. Skyllas-Kazacos, J. Bao, *J. Power Sources* 311 (2016) 57–67. <https://doi.org/10.1016/j.jpowsour.2016.02.018>.
- [21] J. Xu, Q. Ma, L. Xing, H. Li, P. Leung, W. Yang, H. Su, Q. Xu, *Journal of Power Sources* 449 (2020) 227491. <https://doi.org/10.1016/j.jpowsour.2019.227491>.
- [22] W.W. Yang, X.S. Bai, W.Y. Zhang, M.Y. Lu, Q. Xu, *Journal of Power Sources* 457 (2020) 228002. <https://doi.org/10.1016/j.jpowsour.2020.228002>.
- [23] A.A. Shah, M.J. Watt-Smith, F.C. Walsh, *Electrochim. Acta* 53 (2008) 8087–8100. <https://doi.org/10.1016/j.electacta.2008.05.067>.

- [24] H. Al-Fetlawi, A.A. Shah, F.C. Walsh, *Electrochim. Acta* 55 (2010) 3192–3205. <https://doi.org/10.1016/j.electacta.2009.12.085>.
- [25] A.A. Shah, H. Al-Fetlawi, F.C. Walsh, *Electrochim. Acta* 55 (2010) 1125–1139. <https://doi.org/10.1016/j.electacta.2009.10.022>.
- [26] G. Kear, A.A. Shah, F.C. Walsh, *Int J Energy Res* 36 (2012) 1105–1120. <https://doi.org/10.1002/er.1863>.
- [27] P.A. García-Salaberri, T.C. Gokoglan, S.E. Ibáñez, E. Agar, M. Vera, *Processes* 8 (2020) 775. <https://doi.org/10.3390/pr8070775>.
- [28] P. Jienkulsawad, T. Jirabovornwisut, Y.-S. Chen, A. Arpornwichanop, *ACS Sustainable Chem. Eng.* 8 (2020) 13610–13622. <https://doi.org/10.1021/acssuschemeng.0c02973>.
- [29] S. Tsushima, T. Suzuki, *J. Electrochem. Soc.* 167 (2020) 20553. <https://doi.org/10.1149/1945-7111/ab6dd0>.
- [30] C. Yin, Y. Gao, G. Xie, T. Li, H. Tang, *Journal of Power Sources* 438 (2019) 227023. <https://doi.org/10.1016/j.jpowsour.2019.227023>.
- [31] A. Bhattacharjee, A. Roy, N. Banerjee, S. Patra, H. Saha, *J. Power Sources* 396 (2018) 506–518. <https://doi.org/10.1016/j.jpowsour.2018.06.017>.
- [32] A. Clemente, R. Costa-Castelló, *Energies* 13 (2020) 4514. <https://doi.org/10.3390/en13174514>.
- [33] A. Trovò, *Journal of Power Sources* 465 (2020) 228229. <https://doi.org/10.1016/j.jpowsour.2020.228229>.
- [34] Q. Ma, L. Xing, H. Su, W. Zhang, W. Yang, Q. Xu, *Chemical Engineering Journal* 393 (2020) 124753. <https://doi.org/10.1016/j.cej.2020.124753>.
- [35] T. Mannari, T. Okuda, T. Hikihara, *Int J Circ Theor Appl* 2000 (2020) 88. <https://doi.org/10.1002/cta.2881>.
- [36] B. Xiong, Y. Yang, J. Tang, Y. Li, Z. Wei, Y. Su, Q. Zhang, *IEEE Access* 7 (2019) 162297–162308. <https://doi.org/10.1109/ACCESS.2019.2952212>.
- [37] L. Cheng, R.S. Assary, X. Qu, A. Jain, S.P. Ong, N.N. Rajput, K. Persson, L.A. Curtiss, *J. Phys. Chem. Lett.* 6 (2015) 283–291. <https://doi.org/10.1021/jz502319n>.
- [38] S. Er, C. Suh, M.P. Marshak, A. Aspuru-Guzik, *Chem. Sci.* 6 (2015) 885–893. <https://doi.org/10.1039/c4sc03030c>.
- [39] D. Wang, S. Huang, C. Wang, Y. Yue, Q. Zhang, *Organic Electronics* 64 (2019) 216–222. <https://doi.org/10.1016/j.orgel.2018.10.038>.
- [40] D. Zhang, A. Forner-Cuenca, O.O. Taiwo, V. Yufit, F.R. Brushett, N.P. Brandon, S. Gu, Q. Cai, *Journal of Power Sources* 447 (2020) 227249. <https://doi.org/10.1016/j.jpowsour.2019.227249>.
- [41] X. Li, *Electrochimica Acta* 170 (2015) 98–109. <https://doi.org/10.1016/j.electacta.2015.04.075>.
- [42] Q. Chen, M.R. Gerhardt, M.J. Aziz, *J. Electrochem. Soc.* 164 (2017) A1126–A1132. <https://doi.org/10.1149/2.0721706jes>.
- [43] K. Lin, Q. Chen, M.R. Gerhardt, L. Tong, S.B. Kim, L. Eisenach, A.W. Valle, D. Hardee, R.G. Gordon, M.J. Aziz, M.P. Marshak, *Science* 349 (2015) 1529–1532. <https://doi.org/10.1126/science.aab3033>.
- [44] D.G. Kwabi, K. Lin, Y. Ji, E.F. Kerr, M.-A. Goulet, D. de Porcellinis, D.P. Tabor, D.A. Pollack, A. Aspuru-Guzik, R.G. Gordon, M.J. Aziz, *Joule* 2 (2018) 1894–1906. <https://doi.org/10.1016/j.joule.2018.07.005>.
- [45] D.G. Kwabi, Y. Ji, M.J. Aziz, *Chemical reviews* (2020). <https://doi.org/10.1021/acs.chemrev.9b00599>.

- [46] D.R. Conover, V.V. Viswanathan, A.J. Crawford, *Determination of Duty Cycle for Energy Storage Systems Integrated with Microgrids*, 2014.
- [47] K. Soetaert, T. Petzoldt, R.W. Setzer, *J. Stat. Soft.* 33 (2010).
<https://doi.org/10.18637/jss.v033.i09>.
- [48] E. Prada, D. Di Domenico, Y. Creff, J. Bernard, V. Sauvant-Moynot, F. Huet, *J. Electrochem. Soc.* 159 (2012) A1508–A1519. <https://doi.org/10.1149/2.064209jes>.
- [49] M. Petit, E. Calas, J. Bernard, *J. Power Sources* 479 (2020) 228766.
<https://doi.org/10.1016/j.jpowsour.2020.228766>.
- [50] K. Bromberger, J. Kaunert, T. Smolinka, *Energy Technology* 2 (2014) 64–76.
<https://doi.org/10.1002/ente.201300114>.
- [51] K.W. Knehr, E.C. Kumbur, *Electrochem. Commun.* 13 (2011) 342–345.
<https://doi.org/10.1016/j.elecom.2011.01.020>.
- [52] J.R. Rumble Jr., D.R. Lide, T.J. Bruno (Eds.), *CRC handbook of chemistry and physics: A ready-reference book of chemical and physical data, 100th edition 2019–2020*, CRC Press, Boca Raton (Fla.), New York (N.Y.), 2019.
- [53] K.J. Kim, Y.-J. Kim, J.-H. Kim, M.-S. Park, *Materials Chemistry and Physics* 131 (2011) 547–553. <https://doi.org/10.1016/j.matchemphys.2011.10.022>.
- [54] K.J. Kim, H.S. Lee, J. Kim, M.-S. Park, J.H. Kim, Y.-J. Kim, M. Skyllas-Kazacos, *ChemSusChem* 9 (2016) 1329–1338. <https://doi.org/10.1002/cssc.201600106>.
- [55] W. Li, Z. Zhang, Y. Tang, H. Bian, T.-W. Ng, W. Zhang, C.-S. Lee, *Advanced science* (Weinheim, Baden-Wuerttemberg, Germany) 3 (2016) 1500276.
<https://doi.org/10.1002/advs.201500276>.
- [56] C.N. Schmidt, G. Cao, *Sci. China Mater.* 59 (2016) 1037–1050.
<https://doi.org/10.1007/s40843-016-5114-8>.
- [57] A. Fetyan, G.A. El-Nagar, I. Derr, P. Kubella, H. Dau, C. Roth, *Electrochim. Acta* 268 (2018) 59–65. <https://doi.org/10.1016/j.electacta.2018.02.104>.
- [58] Y. Huang, Q. Deng, X. Wu, S. Wang, *International Journal of Hydrogen Energy* 42 (2017) 7177–7185. <https://doi.org/10.1016/j.ijhydene.2016.04.004>.
- [59] M. Gencten, Y. Sahin, *Int J Energy Res* 451 (2020) 629.
<https://doi.org/10.1002/er.5487>.

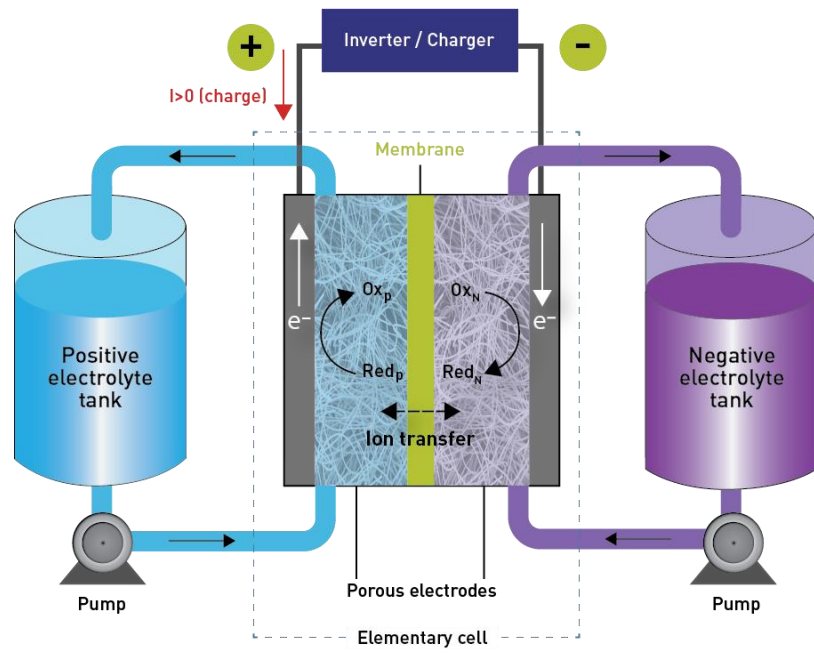


Figure 1: Schematic working principle of RFB

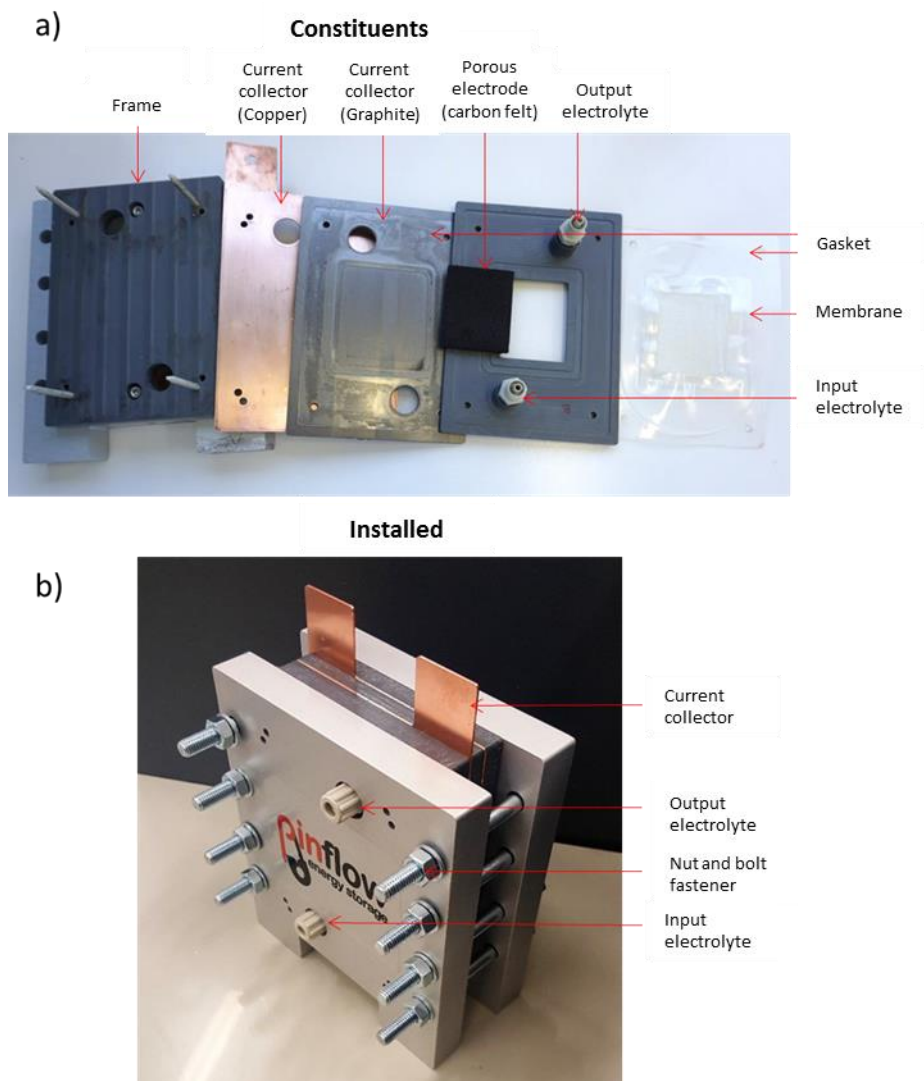


Figure 2: Description of Pinflow redox flow full cell a) constituents, b) installed

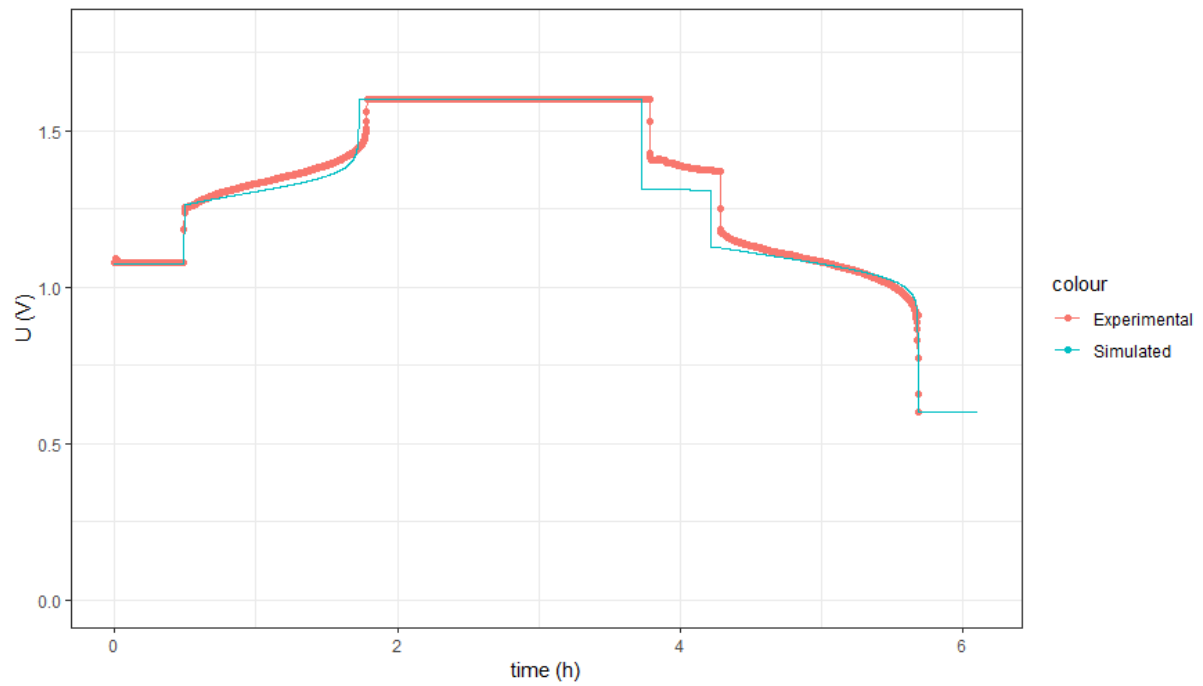


Figure 3: Experimental (O) and optimized simulated (-) cell voltage on a charge/discharge cycle of 2,6-DHAQ/Ferrocyanide battery with $U_{\min} = 0.6$ V, $U_{\max} = 1.6$ V, $I_{\lim} = 50$ mA, $t_{\text{rest}} = 3600$ s and initial conditions given in Table 5

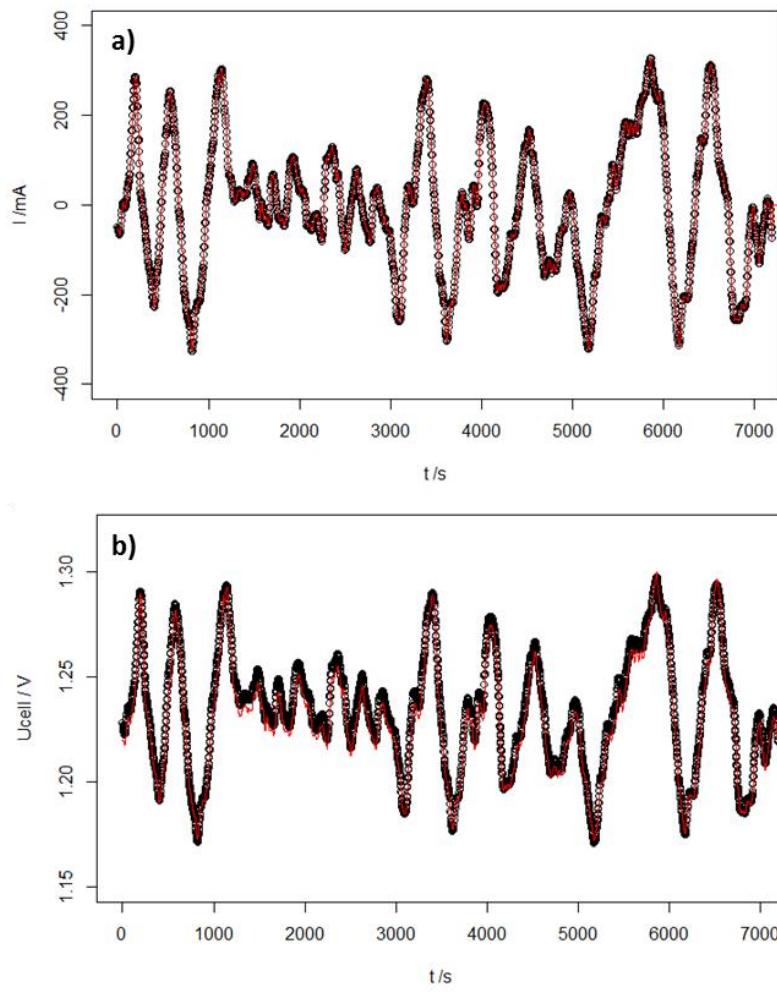


Figure 4: Experimental (o) and simulated (-) a) cell current and b) cell voltage recommended DoE protocol for uniformly measuring and expressing the performance of energy storage systems

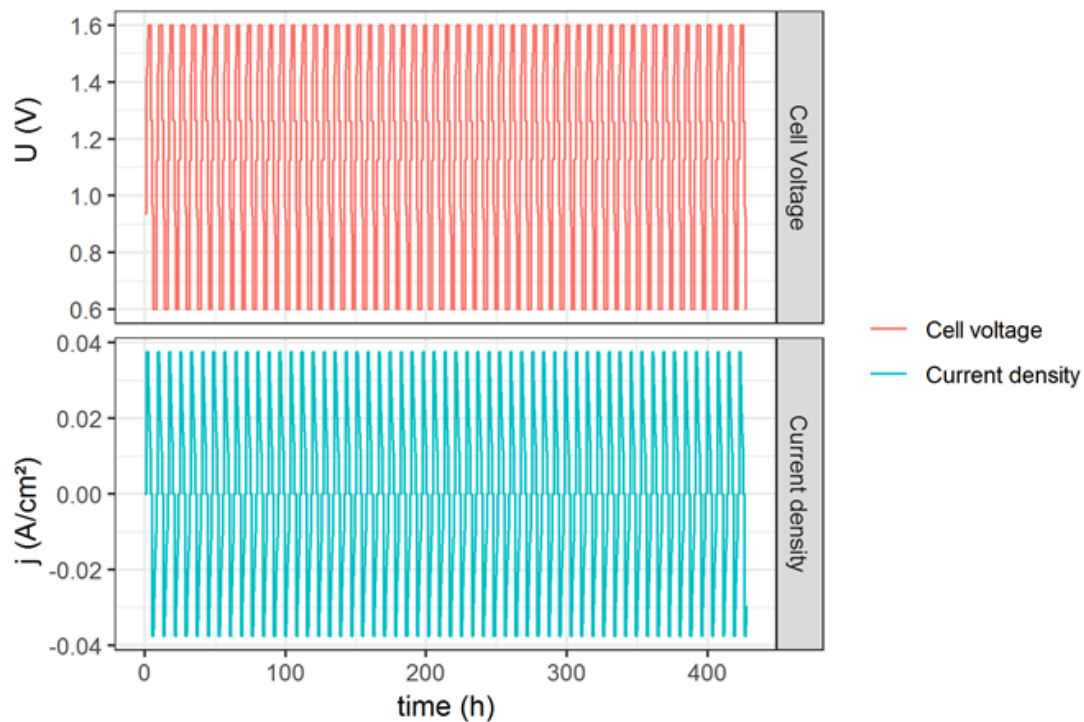


Figure 5: Simulated cell voltage (U) and cell current density (j) during 50 cycles of AORFB with the conditions gathered together in table 2 to 5

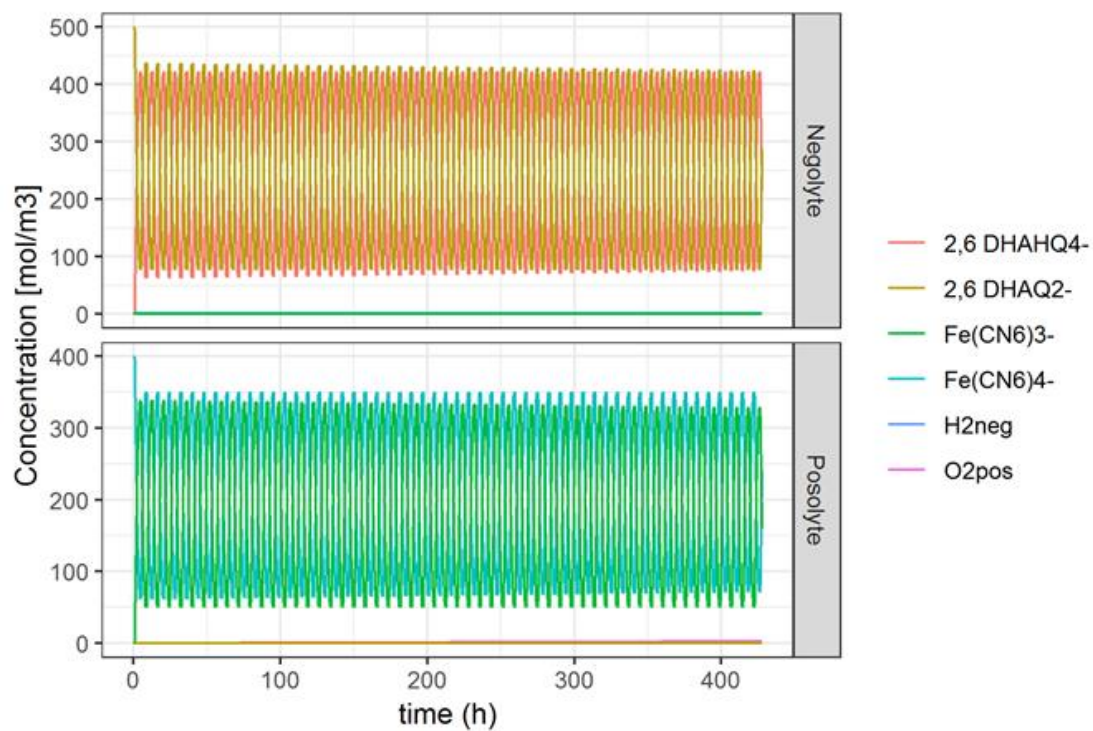


Figure 6: Simulated species concentrations in negolyte and posolyte during 50 cycles of AORFB with the conditions gathered together in table 2 to 5

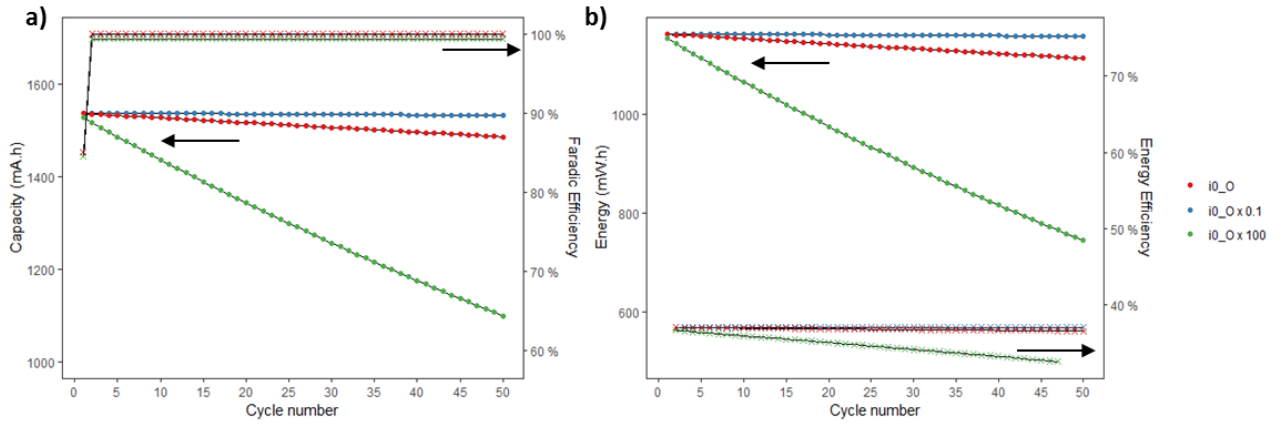


Figure 7: Simulated evolution of a) capacity (●), Faradic efficiency (x), b) energy (●) and energy efficiency (x) up to 50 cycles of AORFB with conditions gathered together in table 2 to 5 and different values of i_O

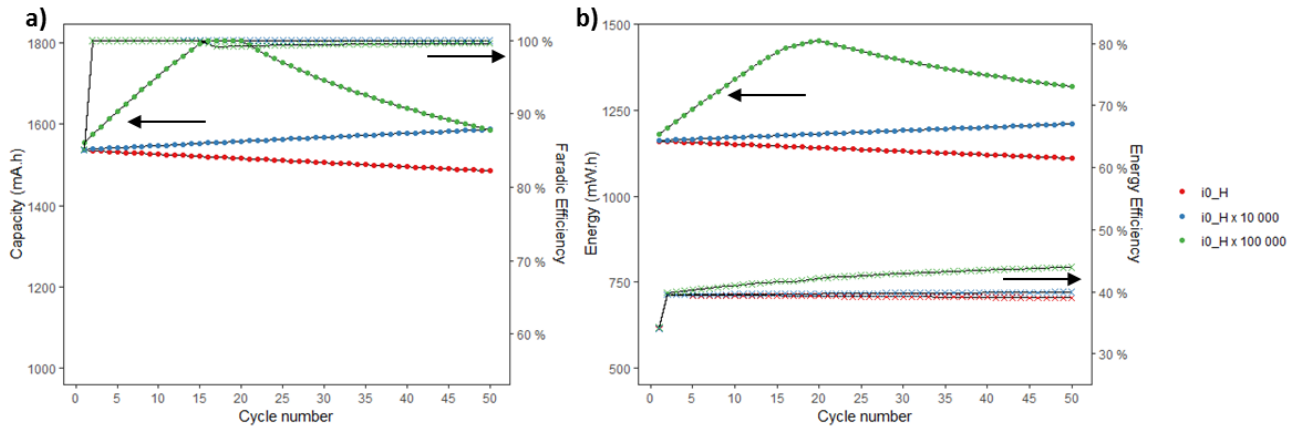


Figure 8: Simulated evolution of a) capacity (●), Faradic efficiency (x), b) energy (●) and energy efficiency (x) up to 50 cycles of AORFB with conditions gathered together in table 2 to 5 and different values of i_H

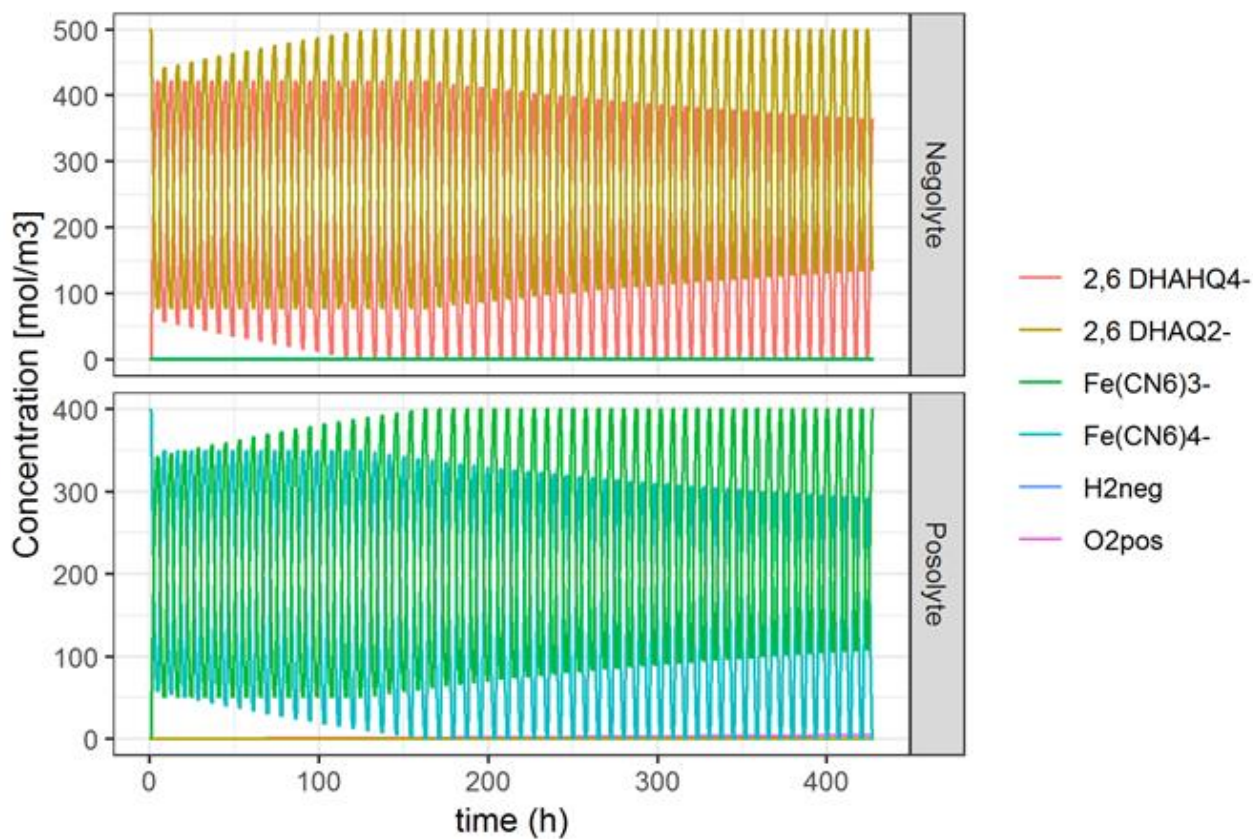


Figure 9: Simulated species concentrations in negolyte and posolyte during 50 cycles of AORFB with the conditions gathered together in tables 2 to 5 excepted i_H which is multiplied by 10^5

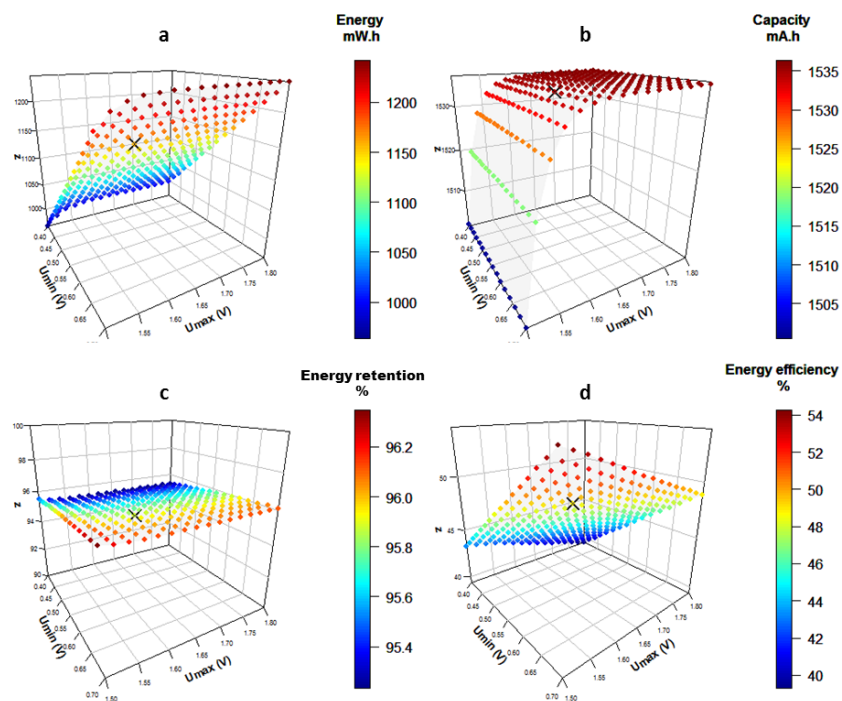


Figure 10: Representation of simulated a) energy at cycle 2, b) capacity at cycle 2, c) energy retention between cycle 2 and 50 and d) energy efficiency at cycle 2 for ORFBs with the conditions gathered together in table 2 to 5 and at different values of U_{min} and U_{max} . X is conditions similar as experimental data (2,6-DHAQ/Ferrocyanide, $U_{min} = 0.6$ V, $U_{max} = 1.6$ V)

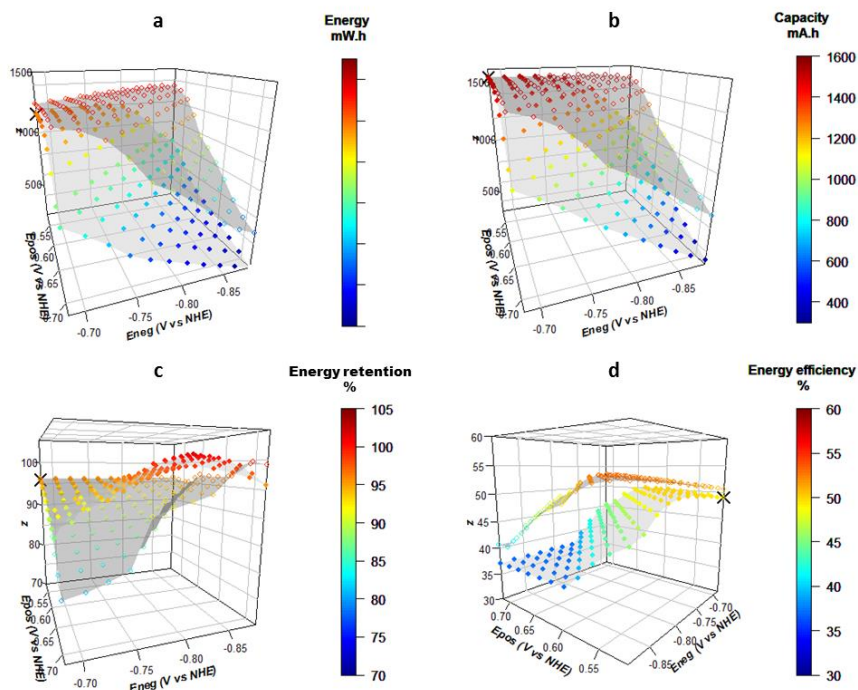


Figure 11: Representation of simulated a) energy at cycle 2, b) capacity at cycle 2, c) energy retention between cycle 2 and 50 and d) energy efficiency at cycle 2 for AORFBs with the conditions gathered together in table 2 to 5 and at different electroactive species with different values of E_{neg} and E_{pos} and for $U_{min} = 0.6$ V and $U_{max} = 1.6$ V (\blacklozenge) and $U_{min} = 0.7$ V and $U_{max} = 1.7$ V (\circ). X is conditions similar as experimental data (2,6-DHAQ/Ferrocyanide, $U_{min} = 0.6$ V, $U_{max} = 1.6$ V)

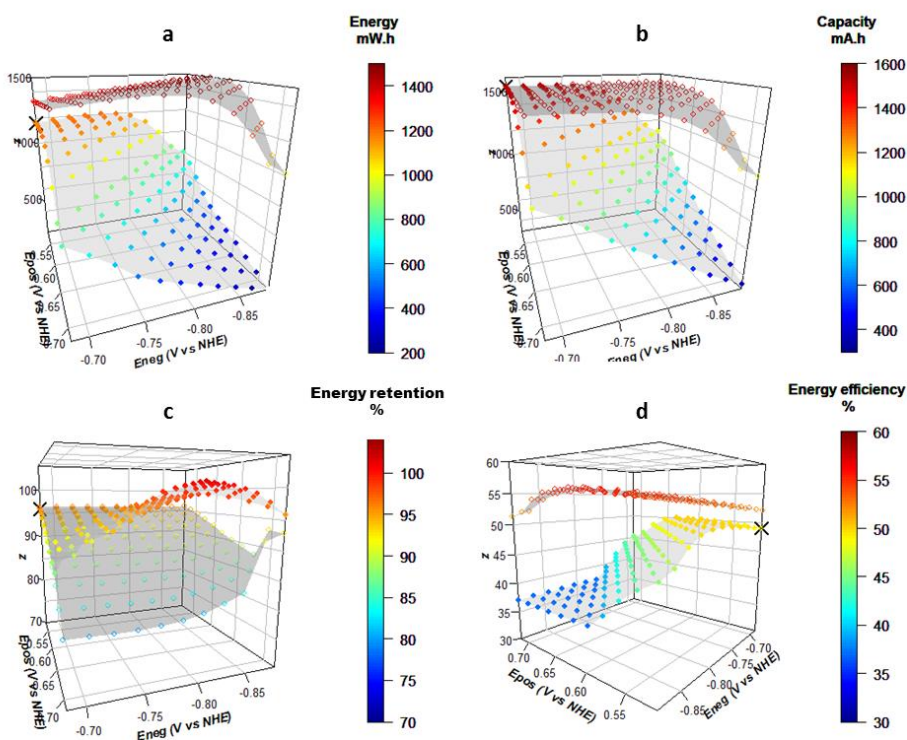


Figure 12: Representation of simulated a) energy at cycle 2, b) capacity at cycle 2, c) energy retention between cycle 2 and 50 and d) energy efficiency at cycle 2 for AORFBs with the conditions gathered together in table 2 to 5 and at different electroactive species with different values of E_{neg} and E_{pos} and for $U_{min} = 0.6$ V and $U_{max} = 1.6$ V (\blacklozenge) and $U_{min} = 0.8$ V and $U_{max} = 1.8$ V (\circ). X is conditions similar as experimental data (2,6-DHAQ/Ferrocyanide, $U_{min} = 0.6$ V, $U_{max} = 1.6$ V)